

Short Note

Source Mechanism and Rupture Directivity of the 18 May 2009

 M_w 4.6 Inglewood, California, Earthquake

by Yan Luo,^{*} Ying Tan, Shengji Wei, Don Helmberger, Zhongwen Zhan, Sida Ni, Egill Hauksson, and Yong Chen

Abstract On 18 May 2009, an M_w 4.6 earthquake occurred beneath Inglewood, California, and was widely felt. Though source mechanism and its location suggest that the Newport–Inglewood fault (NIF) may be involved in generating the earthquake, rupture directivity must be modeled to establish the connection between the fault and the earthquake. We first invert for the event’s source mechanism and depth with the cut-and-paste method in the long-period band (>5 s). Because of the low velocity shallow sediments in the Los Angeles (LA) basin, we use two velocity models in the inversion for stations inside and outside the LA basin. However, little difference is observed in the resolved source mechanism (M_w 4.6, strike $246^\circ/145^\circ$, dip $50^\circ/77^\circ$, rake $17^\circ/138^\circ$) and depth (7 to ~ 9 km), compared to an inversion using the standard southern California model. With the resolved source parameters, we calibrate the amplitude anomaly of the short-period (0.5–2 Hz) P waves with amplitude adjustment factors (AAF). These AAFs are used as corrections when retrieving source mechanisms of the smaller aftershocks using short-period P waves alone. Most of the aftershocks show similar source mechanisms as that of the mainshock, providing ideal empirical Green’s functions (EGFs) for studying its rupture process. We use a forward modeling approach to retrieve rupture directivity of the mainshock, consistent with movement on the NIF with rupture toward the southeast. Although we focus on P waves for analyzing rupture directivity, the resolved unilateral pattern is also confirmed with the azimuthal variation of the duration of SH waves observed in the basin. The high rupture velocity near the shear velocity and relatively low stress drop are consistent with the hypothesis of rupture on a mature fault.

Online Material: Figures illustrating the resolution of earthquake source mechanism and rupture directivity with broadband waveforms.

Introduction

On 18 May 2009, an M_w 4.6 earthquake occurred beneath Inglewood, California (referred to as Inglewood earthquake hereafter; Fig. 1a). It was a few kilometers from the Los Angeles Airport and was felt as far as San Diego and Palm Springs (Fig. 1a,b). The earthquake was assigned M_L 5 initially but later was downgraded to M_w 4.6. Because its location is close to the Newport–Inglewood fault (NIF) and one of the fault planes from the focal mechanism solution has a similar strike to that of the fault, the Inglewood earthquake

is hypothesized to have ruptured on this fault (Fig. 1c). However, early aftershocks (from the Southern California Seismic Network, [SCSN] catalog; see [Data and Resources](#)) do not show obvious alignment along the fault, thus making it difficult to establish the association of the earthquake with the fault.

The NIF is active and can generate at least an M 6.5 earthquake, as manifested by occurrence of the 1933 M_w 6.4 Long Beach earthquake along the southern segment of the fault ([Hauksson and Gross, 1991](#)). However, seismic hazard along the northern segment still needs more examination. Though the fault is assumed to be responsible for at least five M 4.9 or stronger events in the past century, including

*Also at Mengcheng National Geophysical Observatory, School of Earth and Space Sciences, University of Science and Technology of China, Hefei, Anhui, China, 230026.

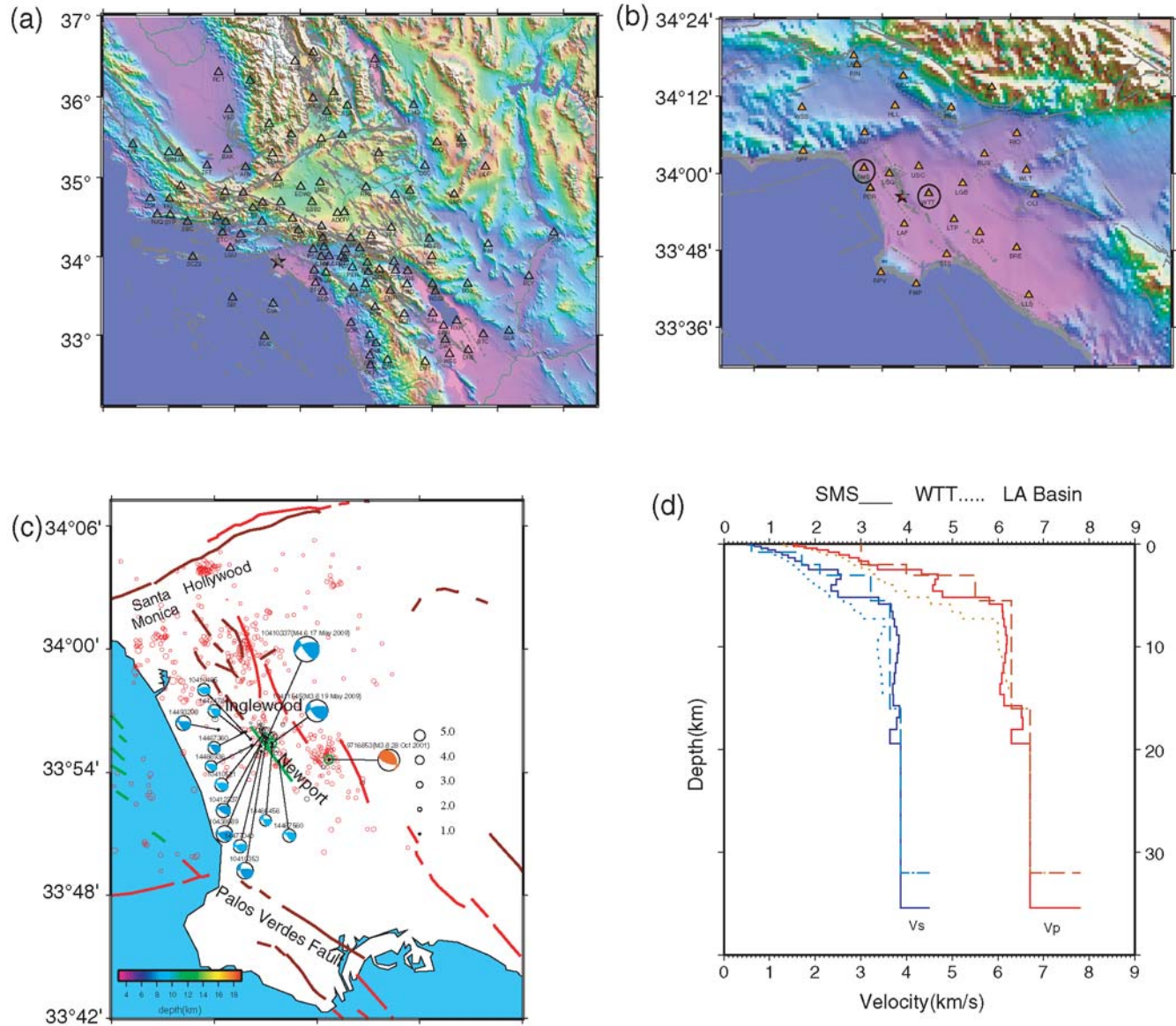


Figure 1. Distribution of Southern California Seismic Network (SCSN) stations and models used in studying the 2009 (M_w 4.6) Inglewood earthquake sequence. The upper panels display (a) the SCSN stations and (b) enlarged Los Angeles basin region with highlighted stations SMS (northwest) and STS (southeast). (c) The Newport–Inglewood fault zone and mechanisms derived in this paper. Blue solid circles denote locations of the Inglewood aftershocks from the SCEC catalog (see Data and Resources), while red and black circles denote historical events and aftershocks relocated with the double-difference method. Three models are displayed in (d), the 1D basin model, and two samples of the 3D SCEC model beneath stations SMS and WTT. The basin model is used in inverting waveforms for the stations displayed in (b).

the 1920 M_L 4.9 event occurring almost at the same location (Hauksson, 1987). Rupture properties of historical events are difficult to determine due to the lack of a dense seismic network, which is indispensable for precise location of earthquake sequences. Even with dense networks (Fig. 1a,b), it is still a challenging task to resolve rupture directivity of M 5 and weaker events because these events have very short duration (≤ 1 s) and the azimuthal variation of waveform due to source finiteness is small.

For such moderate or weaker events, the detailed source process or rupture directivity can only be reliably resolved

with the empirical Green's function EGF approach (e.g., Mori, 1996). Chen *et al.* (2005) proposed an approach of modeling source finiteness based on three-dimensional (3D) waveform modeling of finite moment tensors, but they also found that more accurate solutions are obtained when main-shock and aftershocks are modeled jointly so as to alleviate 3D effects. Instead of the commonly used deconvolution technique, Tan and Helmberger (2010) developed a forward modeling approach to resolve rupture directivity of earthquakes in the 2003 Big Bear sequence. This forward modeling approach can effectively use both the amplitude and

duration information from rupture directivity, provided well-known mechanisms of the target event and the EGF event are available. They first obtain source parameters (moment magnitude, depth, fault planes) of M 4 events by inverting long-period body waves and surface waves with the cut-and-paste (CAP) method (Zhao and Helmberger, 1994; Zhu and Helmberger 1996) and then calculate the AAF (the ratio of synthetic and observed short-period P waves). Thus, they were able to obtain source mechanism of M 2 earthquakes by inverting short-period P waveforms.

Data and Analysis

From the Southern California Earthquake Data Center, we collect broadband waveforms of the mainshock and its 13 largest aftershocks, as well as a nearby M 3.8 event that occurred on 28 October 2001 (Fig. 1c). For the mainshock, broadband velocity records are clipped for stations close to the epicenter, where we used the acceleration records instead. All the records were converted to velocity by removing instrument response. For the mainshock, all the records show high signal-to-noise ratio waveforms at both broadband and short-period (0.5–2 Hz) band, but the most of the aftershocks have strong signals at short periods.

We model the waveforms recorded by stations inside the Los Angeles (LA) basin (Fig. 1b) with basin models (Wen and Helmberger, 1997) and use the southern California one-dimensional (1D) model (Hadley and Kanamori, 1977) to model data recorded at stations outside the LA basins (Fig. 1a). When we calculate Green's functions for stations in the LA basin, we use 1D velocity models extracted from the Southern California Earthquake Center (SCEC) CVM4.0 3D model at each site of the corresponding stations (Magistrale *et al.*, 2000). As displayed in Figure 1d, all the basin models show very low velocity near the surface, and the velocities increases rapidly with depth until reaching the basement interface (about 6 km; i.e., stations SMS and WTT).

Source Parameters of the Mainshock from Long-Period Waveform Modeling

In the CAP approach, three component seismograms are broken into Pnl and surface wave segments and modeled separately. Because differential time shifts are allowed among the different segments, reliable source estimates can be achieved with imperfect Green's functions. Although CAP has been applied successfully in many previous studies, this feature is examined in a recent study by Templeton *et al.* (2008). They first compute synthetic seismograms for a 3D model and invert them for the source mechanism using CAP and assuming 1D Green's functions. They found that the source mechanism from the inversion agrees well with the input source mechanism. The partition methodology of CAP is also used in modeling with 3D synthetic seismograms (Liu *et al.*, 2004). Here, the Green's functions are computed using a reflectivity code (Zhu and Rivera, 2002) for the various 1D

models. We filtered the Pnl waves with a band-pass filter of 0.02–0.2 Hz and surface waves with 0.01 to \sim 0.1 Hz, which are typically adopted for earthquakes in southern California (Tan, 2006). At these frequency bands, typical 3D crustal heterogeneities outside the basins mostly affect travel times of waves (Tan *et al.*, 2010).

After the Green's functions are computed, the CAP method finds the optimal magnitude, fault plane, and centroid depth via grid search. For the 2009 Inglewood earthquake, an M_w of 4.6 is found with a strike of 145° , dip of 77° , and rake of 138° . Error of strike, dip, and strike are estimated to be within 10° , based on sensitivity analysis of fault parameter on waveform misfit, which are calculated during the process of grid searching. The fault plane solution (④ see fig. S1, available in the electronic supplement to this note) shows a source mechanism that is consistent with the seismotectonics inferred from fault plane solutions of events from 1973 to 1985 (Hauksson, 1987). Though the centroid depth (8 km) is shallower than the depth provided by the SCSN catalog (13.6 km), it is deeper than the depth of 5 km from the SCEC's centroid moment tensor. The depth of 5 km is probably too shallow because the basement is at a depth of probably 5 to \sim 6 km from the SCEC CVM4.0, and most tectonic earthquakes are hypothesized to occur in the basement. With two 1D models (a basin model and a background model), Hauksson (1987) found that earthquakes along the NIF cluster at depth range of 6 to \sim 11 km, and our depth estimate of 8 km is in this range. Typically, CAP inversion provides well-resolved centroid depth because the depth is constrained from the amplitude ratio of surface wave-to-body wave, as well as from depth phases in the Pnl wavetrains.

Because the S velocity of the unconsolidated sediments could be very low (down to 300 m/s), hypocenter depth could be biased by very anomalously late S arrivals if both P and S arrivals recorded by near-field basin stations are used in locating the hypocenter. To constrain the accurate depth of the mainshock, we need to model detailed waveforms of P waves, S waves, and converted phases associated with the basin-basement interface, which confirms the depth estimate of 8 km and will be addressed later in this note.

We also invert for source parameters for the largest aftershock (M_w 3.8, event id 10411545) and the 28 October 2001 event (M_w 3.8, event id 9716853) with CAP at long periods. Source mechanism of event 10411545 is very similar to that of the 2009 Inglewood mainshock, and event 9716853 appears to have a thrust mechanism with the strike of one fault plane parallel to the NIF.

Source Parameters of the Aftershocks with Short-Period Waveform Modeling

For an earthquake with sufficiently strong long-period signals (typically $M_w \geq 3.5$ in southern California), the CAP method can be readily applied to infer source mechanisms. However, for weaker events (M 2–3), only short-period body waves are strong enough to escape the noise. Though Ebel

and Bonjer (1990) demonstrated that short-period P and S waves can be used to constrain focal mechanism, the accuracy of the solution depends on the adequacy of the velocity model; for example, Tan and Helmberger (2007) find that the amplitude of observed short-period P waves can be different from synthetics by a factor of 5. Although directly modeling the short-period P waves is difficult without a detailed

velocity model, Tan and Helmberger (2007) demonstrate the amplitude anomaly can be calibrated with well-known events and then corrected in studying smaller events nearby. These so-called AAFs are mainly due to the site effect underneath the stations. For the 2009 Inglewood sequence, we also investigate amplitude variability of short-period P waves. In Figure 2, we overlay synthetic P waves on observed P waves

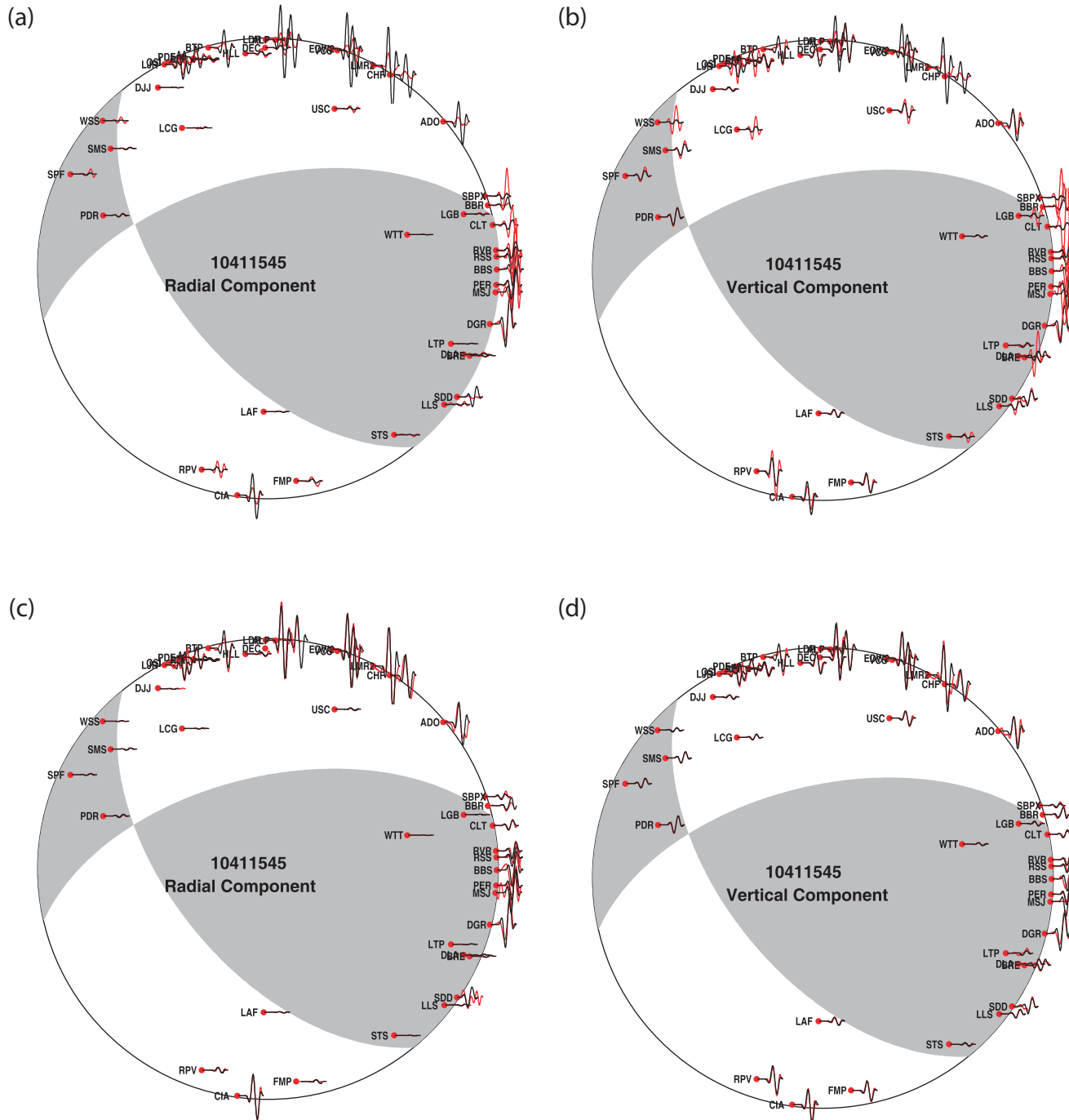


Figure 2. Comparison of short-period (0.5–2 Hz) waveform fits before and after AAF corrections plotted on a focal mechanism projection (lower hemisphere). (E) The differences in mechanisms obtained with and without corrections are displayed in fig. S3 in the electronic supplement to this article.

for the mainshock, event 10411545. The synthetics are computed with source parameters obtained from long-period CAP inversion, then both synthetic and observed P waves are filtered between 0.5 and 2 Hz. Obviously for many of stations, the synthetic P waves are either too large or too small, which is consistent with the study by [Tan and Helmberger \(2007\)](#). However, after we scale the synthetic P waves to the observed ones with a constant (also called an amplitude adjustment factor, AAF), the synthetic and observed P waves match well (Fig. 2c,d), which supports the validity of the approach. In order to obtain more stable AAF estimations at a station, we take the average of AAF at the station for three events; that is, the mainshock, event 10411545, and event 9,716,853. The AAFs of the stations inside the LA basin are mostly above 1, implying basin amplification (Fig. 3).

After the amplitude variability of short-period P pulses are calibrated with AAF, the P amplitude can be readily applied to resolve moment and focal mechanisms. First, we validate that the focal mechanism of the three large events can be recovered with only short-period P waves, which is indeed the case as shown in Figure 3. However, if the P amplitudes are not calibrated, the focal mechanism is noticeably different from that of long-period focal mechanisms. An

example of inverting for the source mechanism of a weak earthquake is displayed in figure S2 (§ available in the electronic supplement to this note). Focal mechanisms of 11 aftershocks (magnitude $M \geq 2$) are inverted with amplitude after calibration, and most of the aftershocks show a similar focal mechanism to that of the mainshock (Fig. 1c), with the strike of one of the fault planes parallel to that of the NIF.

Rupture Directivity of the Mainshock with Short-Period Waveform Modeling

[Tan and Helmberger \(2010\)](#) developed a forward modeling technique that fully utilizes both duration and amplitude information to estimate rupture directivity. The *a priori* Haskell source model proves appropriate for most events that they have studied of the 2003 Big Bear sequence and facilitates estimation of rupture parameters, such as fault length (fl) and rupture speed (V_r).

Here we will follow their approach to study rupture directivity of the mainshock. We select a smaller aftershock, event 10411545 ($M_w \sim 3.5$), as the EGF event. In particular, we conduct a grid search to solve for a common rise time τ_r

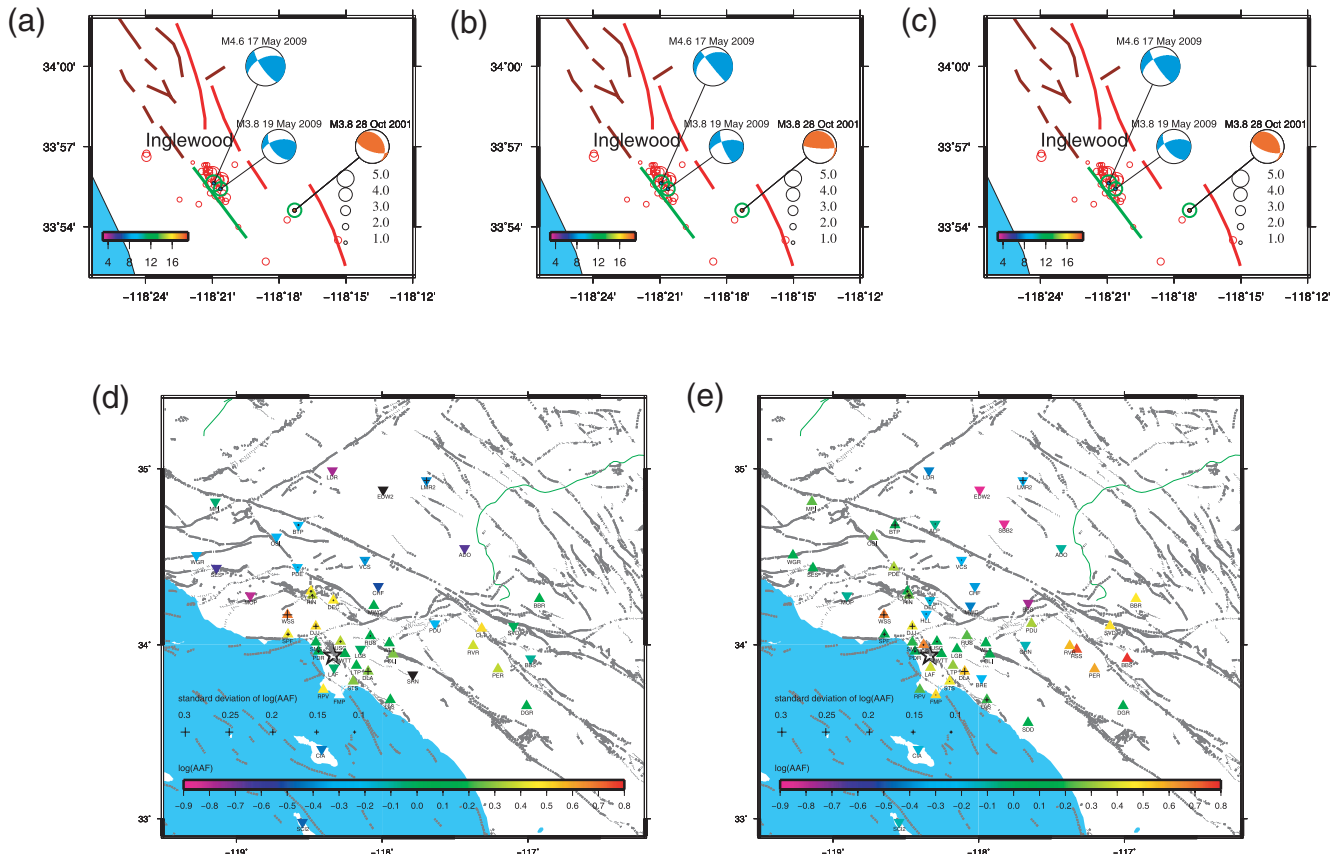


Figure 3. Comparison of focal mechanisms from (a) long-period PnL and surface waves, (b) short-period, and (c) applying AAFs. The averaged AAFs for the (d) vertical and (e) radial components are from three calibration events. Some stations do not have standard deviation estimates because they have an AAF for only one earthquake. Triangles display the negative log(AAF) values, inverse triangles indicate positive log(AAF) values, and the size of the crosses indicates the standard deviation of log(AAF).

and rupture duration time τ_c at individual stations that minimize the total waveform misfit error

$$e = \sum_{i=1}^N [d_i(t) - \Delta M_0 g_i(t) \otimes (\tau_r \otimes \tau_c)]. \quad (1)$$

Here $d_i(t)$ and $g_i(t)$ represent records from the mainshock and the EGF event. ΔM_0 is a scaling factor to account for the two events being different in size and radiation pattern, if applicable. The summation is over the available stations. Note that $\tau_r \otimes \tau_c$ gives the relative source time function of the mainshock with respect to the aftershock. In the simple scenario of unilateral horizontal rupture on a vertical fault, the variation of τ_c can be modeled with

$$\tau_c = \frac{fl}{V_r} - \frac{fl}{V_{p,s}} \cos(\varphi - \phi), \quad (2)$$

where fault length (fl) and rupture speed (V_r) can be easily estimated. φ and ϕ in equation (2) are the rupture propagation direction and the station azimuth, respectively.

We obtain the best rise time fit of 0.24 s, as displayed in Figure 4. The corresponding values for τ_c show large azimuthal variation with a clear minimum near 147° . We follow the same procedure as Tan and Helmberger (2007) for estimating the rupture propagation direction φ , fault length fl , and rupture speed V_r . The obtained φ nearly coincides with the strike of the southeast fault plane of the focal mechanism solution, as well as the NIF. This suggests that the rupture does occur on the NIF and propagates toward the southeast.

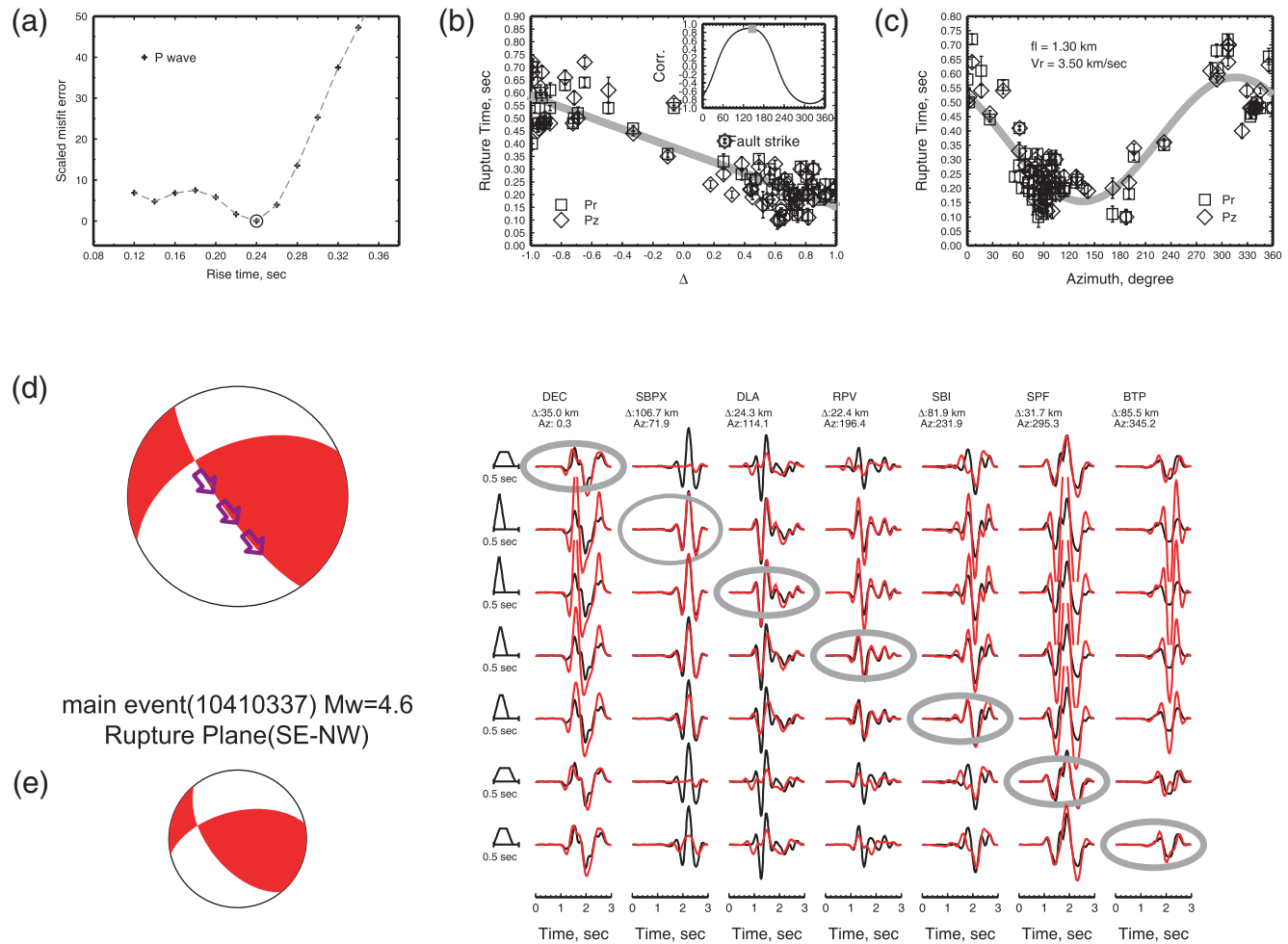


Figure 4. Rupture directivity analysis for the main event. (a) The best fitting STF is found by a grid search, where each P wave is compared against that observed for various assumed rise times and rupture times. The best rise time = 0.24 s, which is determined by summation of misfit errors versus rise time. (b) The corresponding rupture time estimates from P waves where $\Delta = \cos(\varphi - \phi)$ from the preferred rupture propagation direction ϕ . ϕ is chosen where the linear cross-correlation coefficient between rupture time, and Δ reaches the maximum with the estimates of fault length and V_r (rupture velocity), indicated in (c). The gray line displays the linear least-squares fit, from which fault length and rupture speed can be estimated. We used several aftershocks with similar results. (d) The plotted data points are associated with waveform cross-correlation values greater than 0.85 between the main event. (e) The uncertainties of the rupture times are estimated by a 10% decrease in variance reduction.

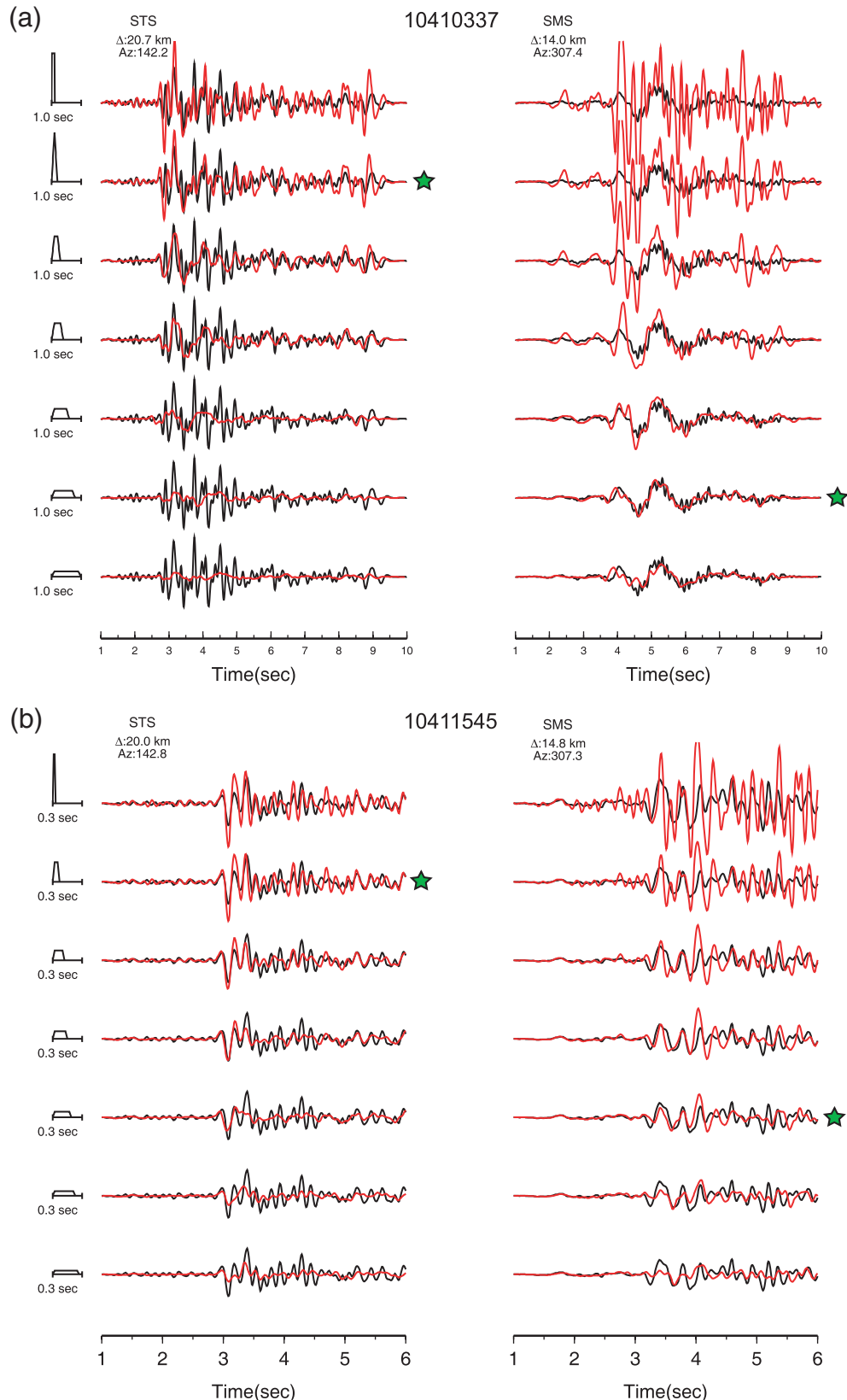


Figure 5. Directivity validation test with two stations along extensions of the strike directions, toward STS and away from SMS, respectively (see Fig. 1b). Various trapezoidal shapes are used to simulate (a) the main event and (b) the largest aftershock. The predictions are given by stars based on the P -wave results. The event pairs are nearly identical at STS after multiplying by ΔM_0 (first columns), while being distinctly different at SMS until corrected for directivity.

Rupture along the NIF is also consistent with relocated aftershocks (black circles, Fig. 1). Assuming a P wave velocity of 6.5 km/s, we obtain a fault length of ~ 1.3 km and a relatively high rupture speed of 3.5 km/s. Accuracy of fault length estimation depends on how well the rupture times can be fit with equation (2). As shown in Figure 4c, the standard deviation is about 0.02 s, which translates into an error of rupture length of $6.5 \text{ km/s} \times 0.02 \text{ s} \sim 0.13 \text{ km}$ (i.e., a 10% error in this case).

We also calculated the stress drop of the event using $\Delta\sigma = M_0/fL^3$. We obtain a low value of 4.5 MPa. The high rupture speed fits the inverse relationship between $\Delta\sigma$ and V_r , found in Tan and Helmberger (2007, 2010), namely that high rupture velocities appear to be associated with low stress drops. We also modeled rupture directivity of event 10411545 with event 10412337 as the reference event. Event 10411545 also ruptures toward the southeast with parameters close to that of the mainshock (figure S3; \oplus available in the electronic supplement to this note). Because this event also ruptures unilaterally, its finite rupture dimension may bring error in estimation of rupture dimension of the mainshock (the true rupture length of the mainshock is then $1.30 \text{ km} + 0.32 \text{ km} = 1.62 \text{ km}$). However, because these two events rupture in the same direction with similar rupture speed, rupture length and rupture time of the mainshock should be affected in the same way (the true rupture time of the mainshock is then $0.37 \text{ s} + 0.07 \text{ s} = 0.44 \text{ s}$), and thus the rupture speed estimate of the mainshock is not much affected ($1.62 \text{ km}/0.44 \text{ s} = 3.7 \text{ km/s}$, an error of 0.2 km/s as compared to 3.5 km/s).

Discussion

We have conducted a waveform modeling study to infer source parameters of the 2009 Inglewood earthquake sequence. Because the LA basin shows substantial lateral variation, one may doubt the effectiveness of 1D modeling. The 3D structure of sedimentary basin does not necessarily produce very large body wave complexities that arrive at stations vertically. Figures S4 and S5 (\oplus available in the electronic supplement to this note) show examples of seismograms computed for 3D basin velocity models.

The rupture velocity of 3.5 km/s for the 2009 M_w 4.6 Inglewood earthquake seems high and has to be confirmed with independent evidence. Because the rupture velocity is inferred from P waves, S waves would provide independent data to verify the rupture directivity. More importantly, the S wave is a better seismic phase for studying rupture velocity because the smaller propagation speed of S waves and the radiation pattern are more favorable than for P waves (Tan and Helmberger, 2007). For the Inglewood earthquake, we choose two stations STS and SMS, which are situated toward and against the rupture direction, respectively (see Fig. 1b). Because the earthquake ruptures toward station STS with a high rupture velocity, the S waveform at STS should be short and have a large amplitude. Similarly, the S wave at station

SMS should be long and weak. It is indeed the case, as displayed in Figure 5a, where event 10411545 is used as an empirical Green's function to compute synthetic seismograms (red). For station STS, a short source duration (second top trace) is required to fit the data (black), while, for station SMS, a longer source duration is needed (second from bottom). Therefore S waves also support the model of high rupture velocity toward the southeast. A similar pattern is also observed for event 10411545, with event 10412337 as reference event (Fig. 5b). The high rupture velocity may be related to the fact that the NIF is a well-developed fault, as discussed by Tan and Helmberger (2010) for the Big Bear sequence.

Twelve events in the 2009 Inglewood sequence mostly show mechanisms of a mixture of strike-slip and thrust, consistent with the result of Hauksson (1987) that six events of strike-slip faulting and seven events of thrust faulting mechanisms occurred along the north segment of NIF. None of the 2009 sequence shows normal faulting mechanism, supporting Hauksson's (1987) theory that only the north section of the NIF is in compression while the southern section is in extension. Another important feature is that the mainshock and event 10411545 both rupture unilaterally with high rupture velocity, which has significant implication for ground motion simulations of a potential future damaging earthquake on the NIF. Areas will experience much higher amplitude of ground motion as the earthquake ruptures toward them.

Conclusions

We have modeled source mechanisms and rupture directivity of the 2009 Inglewood earthquake sequence, which was achievable because the short-period waves are well calibrated. We succeeded in modeling the amplitude of direct P or S waves, but secondary arrivals are much more difficult to model. Some of the secondary arrivals could be generated by basement interfaces as suggested in figure S4 and figure S5 (\oplus available in the electronic supplement to this note). With better 3D models available, it can be expected that both the direct and secondary body waves can be well modeled at short-period frequency or at higher frequency (say, 4 Hz or higher). Thereafter, source parameters of even smaller events ($M < 1$) can be modeled with waveforms at those higher frequencies as discussed by Tan and Helmberger (2007).

Data and Resources

Seismic data used in this article were retrieved with the Seismic Transfer Program from Southern California Earthquake Data Center (<http://www.data.scec.org/>). Plots were made using the Generic Mapping Tools version 4.2.0 (Wessel and Smith, 1998).

Acknowledgments

Supported by the Chinese Academy of Science (CAS) Key Laboratory of Dynamic Geodesy CAS fund kzcx2-yw-116-01, the Institute of Earth Science funding 02092410, China Earthquake Administration funding 200808078, U.S. Geological Survey (USGS) Award No. G09AP00082, and Southern California Earthquake Center (SCEC) Award No. 119938. Data were obtained via the Seismic Transfer Program from the Southern California Earthquake Data Center. Discussion with Hiroo Kanamori helped improve the manuscript. This research was supported by the SCEC, which is funded by National Science Foundation Cooperative Agreement EAR-0529922 and USGS Cooperative Agreement 07HQAG0008. The SCEC contribution number for this paper is 1439; it is Contribution No. 10041, Seismological Laboratory, Division of Geological and Planetary Sciences, California Institute of Technology.

References

- Chen, P., T. H. Jordan, and L. Zhao (2005). Finite-moment tensor of the 3 September 2002 Yorba Linda earthquake, *Bull. Seismol. Soc. Am.* **95**, no. 3, 1170–1180.
- Ebel, J. E., and K. P. Bonjer (1990). Moment tensor inversion of small earthquakes in southwestern Germany for the fault plane solution, *Geophys. J. Int.* **101**, 133–146.
- Hadley, D., and H. Kanamori (1977). Seismic structure of the Transverse Ranges, California, *Geol. Soc. Am. Bull.* **88**, 1469–1478.
- Hauksson, E. (1987). Seismotectonics of the Newport-Inglewood fault zone in the Los Angeles basin, Southern California, *Bull. Seismol. Soc. Am.* **77**, no. 2, 539–561.
- Hauksson, E., and S. Gross (1991). Source parameters of the 1933 Long Beach earthquake, *Bull. Seismol. Soc. Am.* **81**, 81–98.
- Liu, Q., J. Polet, D. Komatsch, and J. Tromp (2004). Spectral-element moment tensor inversions for earthquakes in southern California, *Bull. Seismol. Soc. Am.* **94**, 1748–1761.
- Magistrale, H., S. Day, R. Clayton, and R. Graves (2000). The SCEC southern California reference three-dimensional Seismic Velocity Model version 2, *Bull. Seismol. Soc. Am.* **90**, no. 6B, S65–S76.
- Mori, J. (1996). Rupture directivity and slip distribution of the M 4.3 foreshock to the 1992 Joshua Tree earthquake, Southern California, *Bull. Seismol. Soc. Am.* **86**, no. 3, 805–810.
- Tan, Y. (2006). Broadband waveform modeling over a dense seismic network, *Ph.D. Thesis*, California Institute of Technology, Pasadena, California.
- Tan, Y., and D. V. Helmberger (2007). A new method for determining small earthquake source parameters using short-period P waves, *Bull. Seismol. Soc. Am.* **97**, 1176–1195.
- Tan, Y., and D. V. Helmberger (2010). Rupture directivity of the 2003 Big Bear sequence, *Bull. Seismol. Soc. Am.* **100**, no. 3, 1089–1106.
- Tan, Y., A. Song, S. Wei, and D. Helmberger (2010). Surface wave path corrections and source inversions in southern California, *Bull. Seismol. Soc. Am.* **100**, no. 6, 2891–2904.
- Templeton, D., A. Rodgers, D. Helmberger, and D. Dreger (2008). Comparison of the cut-and-paste and full moment tensor methods for estimating earthquake source parameters, *Eos Trans. AGU* **89** (53), abstract S41C-1864.
- Wen, L. X., and D. V. Helmberger (1997). Propagational corrections for basin structure: Landers earthquake, *Bull. Seismol. Soc. Am.* **87**, no. 3, 782–787.
- Wessel, P., and W. H. F. Smith (1998). New, improved version of generic mapping tools released, *EOS Trans. AGU* **79**, 579.
- Zhao, L., and D. V. Helmberger (1994). Source estimation from broadband regional seismograms, *Bull. Seismol. Soc. Am.* **84**, 91–104.
- Zhu, L., and D. V. Helmberger (1996). Advancement in source estimation techniques using broadband regional seismograms, *Bull. Seismol. Soc. Am.* **86**, 1634–1641.
- Zhu, L. P., and L. A. Rivera (2002). A note on the dynamic and static displacements from a point source in multilayered media, *Geophys. J. Int.* **148**, no. 3, 619–627.

Institute of Earthquake Sciences
China Earthquake Administration
Beijing, China
(Y.L., Y.C.)

Seismological Laboratory
California Institute of Technology
Pasadena, California 91125
(Y.T., S.W., D.H., Z.Z., E.H.)

CAS Key Laboratory of Dynamic Geodesy
Institute of Geodesy and Geophysics
Wuhan, China, 430077
sdni@whigg.ac.cn
(S.N.)

Manuscript received 5 April 2010